Article

A CFD-DEM Model for Particle Transport in Airways

Mohammad S. Islam[1*], Puchanee Larpruenrudee[1], Md. Mizanur Rahman[2], Zhen Luo[1], Emilie Sauret[3], and Yuantong Gu[3]

[1]School of Mechanical and Mechatronic Engineering, University of Technology Sydney (UTS), 15 Broadway, Ultimo, NSW-2007, Australia
[2]School of Engineering, Design and Built Environment, Western Sydney University, Penrith, NSW 2751, Australia.
[3]School of Mechanical, Medical and Process Engineering, Faculty of Engineering, Queensland University of Technology, Brisbane, QLD 4000, Australia.
* Correspondence: mohammadsaidul.islam@uts.edu.au

Abstract: The fluid flow field at the upper airways is highly complex due to the complex structure of the airway. The inhaled particle flow, the air streamline and the interaction of the continuum and discrete phase could significantly affect the transport behaviour of the inhaled particles. A range of analytical, mathematical and computational fluid dynamics (CFD) models analyzed the airflow and particle transport in different idealized and asymmetric airway models. A precise understanding of the continuum and discrete phase interaction in realistic human airways is missing, and this study aims to develop a CFD-DEM model for particle transport in realistic airways. This study uses the CFD model for the continuum phase and the discrete element method (DEM) for the discrete phase. A soft sphere approach is used for the interaction of the discrete phase. Proper validation is performed for particle transport efficiency. The CFD-DEM model analyzed the particle transport in an idealized and realistic airway model, and different methods are used to analyze the transport behaviour. During the particle-particle interaction, a stagnation point and a high-pressure zone are observed at the airway model's carinal angle. The numerical results report higher deposition efficiency (DE) for particle-particle interaction than without interaction. The flow field becomes highly complex with the spring constant values, and higher DE is found for high spring constant values. The spring dashpot friction-dshf method shows higher deposition at the upper part of the airways than other interaction methods. The findings of this study and more case-specific analysis would improve the knowledge of aerosol transport in airways and the health risk assessment of the patient.

Keywords: CFD-DEM; Particle-particle interaction; Upper airway; DE; Spring constant.

Introduction

A precise understanding of the fluid flow and particle transport dynamics in the human respiratory system is important for the respiratory health risk assessment of respiratory patients and the efficient design of the targeted drug delivery devices. Inhalation therapy is usually used to treat chronic obstructive pulmonary diseases and bronchial asthma (Murphy et al., 2000). Inhalation is preferable to oral delivery and injection for drug absorption due to the lung's effective absorption area and thin epithelial cells (Sakagami, 2006). The main advantage of this method is the administration of medications that are difficult to be absorbed, such as peptides, which cannot be absorbed from the gastrointestinal tract. Inhalation can be roughly classified into two types, including metered dosage inhalation and dry powder inhalation. This is technically based on the technique and fundamental principle (Newman, 2005; Telko et al., 2005). In general, for therapeutic activity by inhalation therapy, the inhaled drugs must be deposited in the respiratory system, including the lung and airway mucous (Rahman et al., 2022; Sécher et al., 2019). To ensure that the amount of inhaled drugs is delivered appropriately, it is essential to understand the airflow characteristics, drug transport and deposition within the spe-

 doi:10.20944/preprints202211.0500.v1

cific area along the airway. Because of this reason, realistic models of the human respiratory system are employed to simulate airflow dynamics and related particle deposition through computational fluid-particle dynamics (Koullapis et al., 2018). For the microparticle size drug delivery, most inhaled particles typically deposit before passing into the trachea because of inertial impaction and strong turbulence dispersion in the mouth-throat region (Kleinstreuer et al., 2008). Therefore, particle-particle interaction mechanisms can be ignored in this region because the residual particle suspension is diluted before it enters the tracheobronchial airways (Ghahramani et al., 2014).

Typically, the airway wall is considered as a fully trapped wall for the boundary condition of the particle-wall interaction, as the layers of mucus always cover the inner wall of the human respiratory system (Garcia et al., 2007). Prior research on particle deposition in the human lung mostly used the computational fluid dynamics-discrete phase model (CFD-DPM). Standard Euler-Lagrange methods are usually used for the CFD-DPM as these methods are reliable in such situations for the estimation of particle transport and deposition in lung airways. However, the CFD-DPM does not consider the contact between the fluid, particle, and wall surfaces (Vulović et al., 2018). The interaction between a simulation model's particle surface and particle was disregarded in the CFD-DPM experiment (Islam et al., 2022). In fact, particle-particle and particle-wall interactions are the key factors that significantly affect particle passage and deposition in lung airways, especially when significant levels of air pollutants are breathed or dense pharmaceutical particle suspensions are supplied for targeting the lung (Feng et al., 2014).

To consider the effect of particle-particle interaction, the computational fluid dynamics-discrete element method (CFD-DEM) is one of the appropriate techniques. Based on this technique, the particle's motion will be calculated individually, corresponding to the time during particle travelling inside the airways (Chen et al., 2012; Branco Junior et al., 2015). Then, it will provide the natural particle flow correctly. An idealized pulmonary airway model was applied to examine the properties of particle transportation and deposition under the CFD-DEM for the first time (Chen et al., 2012). From the available literature, most studies only focused on the investigation of airflow patterns, particle transport and deposition within the human lung airways by using the CFD-DPM under a non-realistic lung model and a realistic lung model. The non-realistic lung model was only used for the CFD-DEM. A comprehensive investigation of using CFD-DEM with two-way coupling for dense particle suspension flow in a realistic lung model is still required. Furthermore, requiring two-way interaction are also dense particle-suspension flows along complicated paths. In order to investigate how particle deposition behaves in the respiratory system and their reachability, the CFD-DEM model is employed in computational simulations in the current study by using the realistic central part of the human lung airway. The CFD-DEM model analyses particle transport quantitatively while taking spherical particles and their interactions with the surface of the human respiratory system. The comparison of the effect of the particle-particle interaction on the airflow characteristic and particle deposition between the realistic lung model and the non-realistic lung model is performed in this study. Furthermore, the effect of particle-particle interaction on the airflow patterns and particle deposition is also compared to the case without particle interaction.

Methodology

1. Geometrical Generation

Two geometrical lung models of the central airway were employed in this study and presented in **Figure 1**. These included the non-realistic model and the realistic model. The non-realistic lung model of the central airway was created by using SolidWorks based on Weibel's lung dimension (Weibel 1963). For the realistic model, the 3D model of a central airway was generated from the CT image of the upper airway from 51 years healthy male,

Preprints (www.preprints.org) | NOT PEER-REVIEWED | Posted: 28 November 2022 doi:10.20944/preprints202211.0500.v1

which was used in the previous study (Islam et al., 2019). **Figure 1a** illustrates the symmetric lung model for a non-realistic case, while **Figure 1b** presents the realistic model of the lung at the central airway after proper surface rendering and reconstruction. It should be noted that the left side of the realistic model is referred to as the right lung in reality, as the diameter of this side is larger than another side. Therefore, the right side of this model is referred to as the left lung.

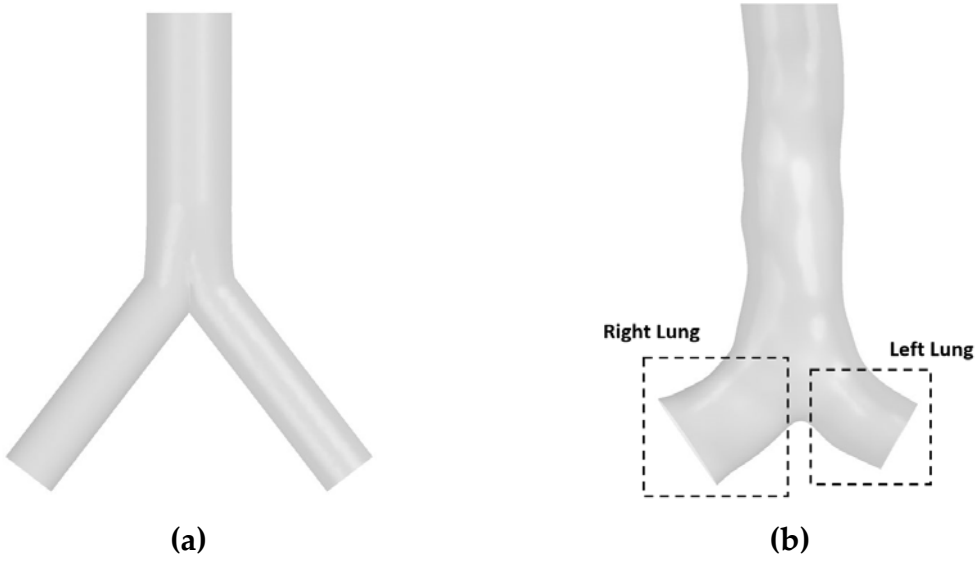

Figure 1. Geometrical models of central airway. (a) non-realistic model and (b) realistic model.

2. Mesh Generation and Validation

The commercial software ANSYS meshing module was used to create unstructured tetrahedral elements with the inclusion of an inflation layer for the mesh treatment at the wall. From this method, the minimum orthogonal quality of the generated mesh is 0.19. The grid refinement test was performed under various parameters, including dynamic pressure at the outlet, velocity magnitude at the inlet, and DE. The results from this test indicated that all of the values from selected parameters were stable at 7.2 million computation elements. To save the computational time, this value was selected for further simulations. More details regarding mesh generation and grid refinement can be found in the authors previous study (Islam et al., 2019). **Figure 2** demonstrates the unstructured mesh for the non-realistic model (**Figure 2a**) and realistic model (**Figure 2b**).

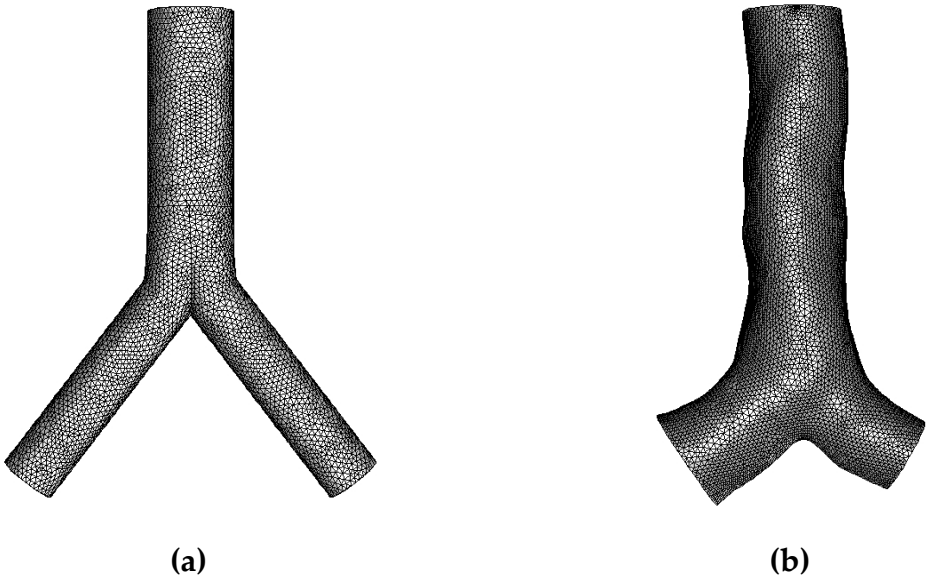

Preprints (www.preprints.org) | NOT PEER-REVIEWED | Posted: 28 November 2022 doi:10.20944/preprints202211.0500.v1

Figure 2. Unstructured mesh of central airway. (a) non-realistic model and (b) realistic model.

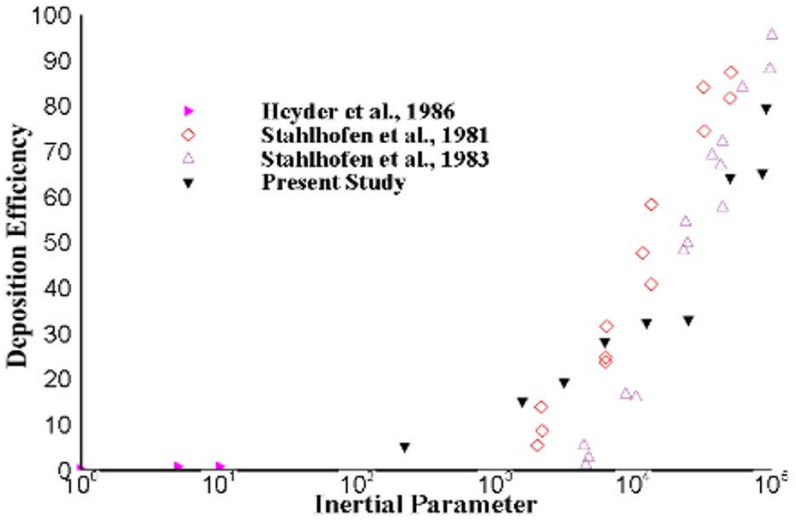

Figure 3. Deposition efficiency (DE) comparison at extrathoracic airway in terms of inertial parameter with available literature (Heyder et al., 1986; Stahlhofen et al., 1981; Stahlhofen et al., 1986).

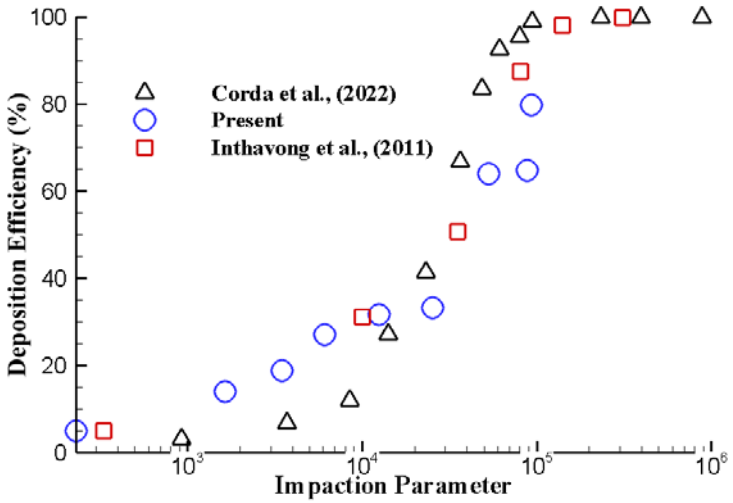

Figure 4. Deposition efficiency (DE) comparison at extrathoracic airway in terms of impaction parameter with available literature (Corda et al., 2022; Inthavong et al., 2011).

Figure 3 and **Figure 4** shows the DE of the microparticle at the extrathoracic airway as a function of inertial parameter. The DE for different inertial parameter values show a good agreement with the available literature.

3. Numerical Methods

The numerical simulation from this study is performed by using ANSYS Fluent based on 3D simulation, pressure-based solver and double precision serial processing model. The effect of particle-particle interaction on the fluid flow patterns and particle transport and deposition is analyzed based on various initial parameters, including flow rates and particle sizes. In the present study, the CFD-DEM is used by considering the fluid flow as the continuous phase for the CFD and particles as discrete particles for DEM.

The governing equations for the continuous fluid flow inside the domain for the CFD are based on the mass and momentum conservations as Equation 1 and 2, respectively.

Preprints (www.preprints.org) | NOT PEER-REVIEWED | Posted: 28 November 2022 doi:10.20944/preprints202211.0500.v1

$$\frac{\partial \rho}{\partial t} + \nabla.(\rho \vec{v}) = 0 \tag{1}$$

$$\frac{\partial}{\partial t}(\rho \vec{v}) + \nabla \cdot (\rho \vec{v} \vec{v}) = -\nabla p + \nabla \cdot \left(\mu \left[(\nabla \vec{v} + \nabla \vec{v}^T) - \frac{2}{3} \nabla \cdot \vec{v} I \right] \right) + \rho \vec{g} + \vec{F} \tag{2}$$

where p is the fluid static pressure, $\vec{g}$ is a body force of gravity, and $\vec{F}$ is a body force of external force (particle–fluid interaction force) which is given by (Chen et al., 2012);

$$\vec{F} = \sum_{1}^{n} \frac{\vec{f}_{D,i}}{\Delta V} \tag{3}$$

where $\vec{f}_{D,i}$ is the drag force exerted on particle i, n refers to the number of particles in the specific computational cell, and ΔV is the volume of the cell.

In the DEM model, the translational and rotational motions of an individual particle in a system are governed by its interactions with neighbouring particles, walls, and surrounding fluid. The governing equations for DEM are described by Newton's second law of motion (Zhu et al., 2007). The present study employs the soft-sphere approach (**Figure 5**) which was originally developed by Cundall & Strack (1979). The motions of individual particles are determined by Equation (4) and Equation (5)

$$m_i \frac{dv_i}{dt} = \sum \left(F_{ij}^n + F_{ij}^t \right) m_i g \tag{4}$$

$$I_i \frac{d\omega_i}{dt} = \sum \left(R_i \times F_{ij}^t - \tau_{ij}^r \right) \tag{5}$$

where m_i, I_i, v_i, and ω_i refer to the mass, moment of inertia, translational, and rotational velocities of particle i, respectively. R_i denotes the vector from the centre of particle i to a contact point where F_{ij}^t is used. F_{ij}^n and F_{ij}^t are normal and tangential contact forces due to the interaction between particle i and j at the current time step. τ_{ij}^r refers to the torque due to rolling friction.

In general, the forces from the inter-particle collision for the soft sphere approach are determined by the deformation or overlap between two particles. By this technique, the particle motion equation is integrated over time to capture the interaction of the particle. A spring constant value for the soft sphere approach can be estimated by several factors, including the collision time, restitution coefficient, and the relative velocity of the colliding particle (Islam et al., 2020).

Preprints (www.preprints.org) | NOT PEER-REVIEWED | Posted: 28 November 2022 doi:10.20944/preprints202211.0500.v1

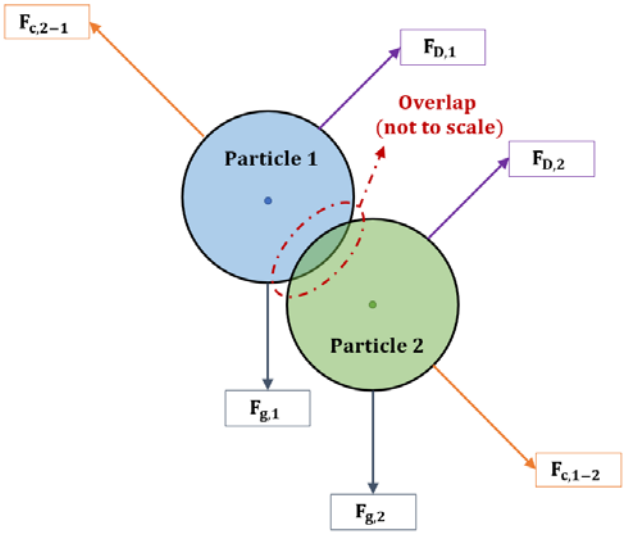

Figure 5. Particle-particle interaction and soft sphere approach.

To calculate the particle contact forces, there are three techniques that can be used. These include the spring collision law, the spring-dashpot collision law, and the friction collision law. To obtain the results, a spring constant is the key parameters for these three techniques. The spring constant (K) can be calculated by using Equation (6).

$$K = \frac{\pi v^2}{3\varepsilon_D^2} D_\rho \tag{6}$$

where D is the parcel diameter, ρ and v are the particle mass and relative velocity between two colliding particles, respectively. ε_D is the fraction of the diameter for allowable overlap. The collision time scale can be defined as $\pi\sqrt{\frac{m}{K}}$, where m is the parcel mass which is defined by $\frac{\rho D^3 \pi}{6}$.

The spring collision law is basically based on a unit vector ($\vec{e}_{12}$) is determined for two particles from the centre of particle 1 and the centre of particle 2 as the following equation;

$$\vec{e}_{12} = \frac{(x_2 - x_1)}{\|x_2 - x_1\|} \tag{7}$$

where x_1 and x_2 are the position of the particle 1 and 2, respectively. The overlap (δ) between two particles during contacting should be less than zero, which is calculated by the following equation;

$$\delta = \|x_2 - x_1\| - (r_1 - r_2) \tag{8}$$

where r_1 and r_2 are the radius of the particle 1 and 2, respectively.

From this technique, the force on particle 1 ($\vec{F}_1$) is calculated by using a spring constant (K) which should be greater than zero. For the force on particle 2 ($\vec{F}_2$), it is depended on the Newton's third law. The force on particle 1 and particle 2 can be calculated by using Equation (9) and Equation (10), respectively.

$$\vec{F}_1 = K\delta\vec{e}_{12} \tag{9}$$

$$\vec{F}_2 = -\vec{F}_1 \tag{10}$$

For the spring-dashpot collision law, a dashpot term ($\eta; 0 < \eta \leq 1$) from the spring-dashpot collision law is defined with spring constant (K) and the coefficient of restitution. The force during the particle collision can be calculated based on the expressions for the

Preprints (www.preprints.org) | NOT PEER-REVIEWED | Posted: 28 November 2022 doi:10.20944/preprints202211.0500.v1

loss factor and so-called reduced mass of the two particles that are defined by the following equation;

$$f_{loss} = \sqrt{\pi^2 + ln^2\eta} \tag{8}$$

$$m_{12} = \frac{m_1 m_2}{m_1 + m_2} \tag{9}$$

The collision timescale (t_{coll}) of the particle and damping coefficient (γ) are determined based on the following equations;

$$t_{coll} = f_{loss}\sqrt{\frac{m_{12}}{K}} \tag{10}$$

$$\gamma = -2\frac{m_{12}\ln\eta}{\sqrt{\pi^2 + ln^2\eta}\sqrt{\frac{m_{12}}{K}}} \tag{11}$$

The relative velocity between particle 1 and particle 2 is defined as;

$$\vec{v}_{12} = \vec{v}_2 - \vec{v}_1 \tag{12}$$

where $\vec{v}_1$ and $\vec{v}_2$ are the velocity of particle 1 and 2, respectively.

Based on this technique, the force on particle 1 is defined as Equation (13), while the force on particle 2 is still based on Equation (9).

$$\vec{F}_1 = (K\delta + \gamma(\vec{v}_{12} \cdot \vec{e}_{12}))\vec{e}_{12} \tag{13}$$

The friction collision law is calculated based on the equation for Coulomb friction ($\vec{F}_{friction}$);

$$\vec{F}_{friction} = \mu\vec{F}_{normal} \tag{14}$$

where, μ is the friction coefficient and $\vec{F}_{normal}$ is the force that is normal to the surface.

It should be noted that most numerical simulations from this study are performed by using this the spring dashpot collision technique. However, the comparision of particle depositons between these three techniques are maded and presented in the results and discussion section.

Under the DEM model, the injection file is applied for the initial locations of released particles along the domain. The boundary conditions are taken as the inlet velocity of the fluid flow at the top surface of the domain and the outlet outflow at the end of the left and right lung sides. The initial velocities at the inlet are various based on the daily physical activities, including 15 lpm, 30 lpm, and 60 lpm. The selected sizes of a spherical particle in this study include 1 μm, 5 μm, and 10 μm. **Table 1** presents the physical input properties of the fluid (air) and aerosol.

Table 1. Properties of air and aerosol.

Properties	Air	Aerosol
Density (kg/m^3)	1.225	1100
Viscosity (kg/m-s)	1.7893×10^{-5}	-

The average total particle count per injection is 1,016 particles for all numerical simulations. The boundary conditions at the wall are set as a stationary wall, with a no-slip

Preprints (www.preprints.org) | NOT PEER-REVIEWED | Posted: 28 November 2022 doi:10.20944/preprints202211.0500.v1

condition and a trap condition to catch the particle when touching the walls. The convergence criteria of the continuity and momentum equations are set as 0.0001.

1. Airflow Analysis

1.1. Velocity Analysis

The velocity analysis in this section is focused on the comparison of the flow characteristics between the different lung geometries and selected parameters of the DEM model.

1.1.1. Velocity Analysis for non-realistic model and realistic model

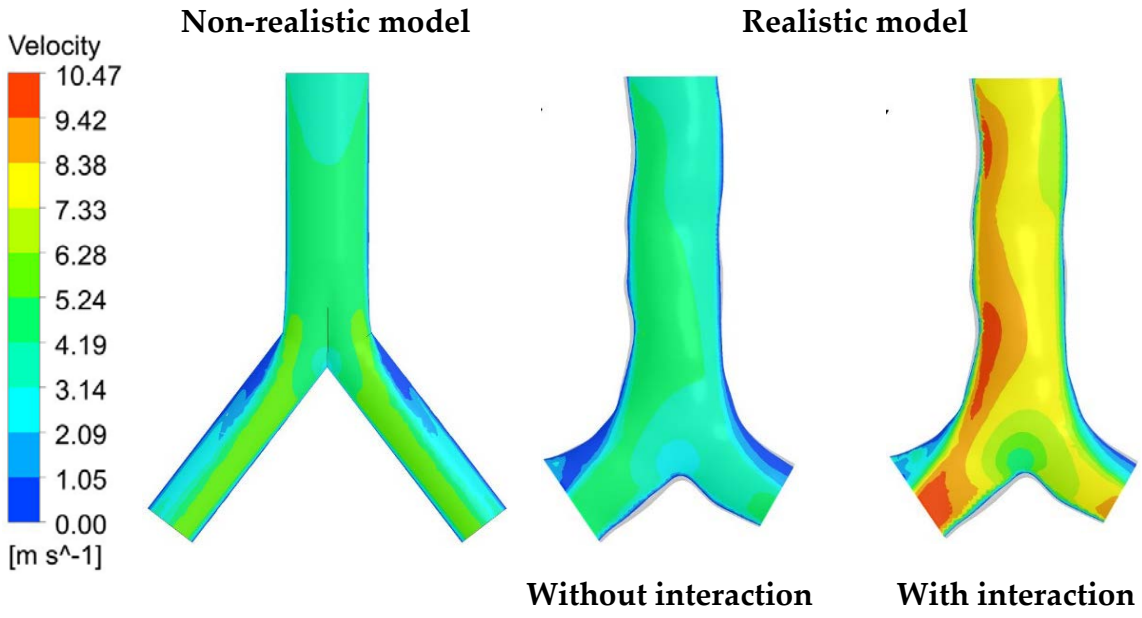

Figure 6. Velocity contour at X-Y Plane for 60 lpm flow rate between non-realistic model and realistic model.

Figure 6 presents the comparison of velocity magnitude along the velocity contour at the X-Y plane between the non-realistic model and realistic model under the 60 lpm flow rate. Furthermore, the difference in flow velocity between particle interaction and without particle interaction is also presented in this figure. From this figure, it can be seen that the lower and lowest velocity magnitudes were found at nearly the upper wall of the left and right sides of these models. Considering the flow pattern inside the bifurcation between these models, the flow patterns from the realistic model with and without particle interaction are similar, but these patterns are different from the non-realistic model case. This is because of the change of cross-sectional area in the realistic model, which generates the vortices during fluid flows inside the bifurcation. A highly asymmetric anatomical model from a realistic case significantly generates a higher flow distribution during flowing inside the bifurcation. However, the velocity magnitude of the bifurcation between the non-realistic model and the realistic model without particle interaction is quite similar, as the maximum velocity magnitude from these two models is lower than 7.33 m/s. The higher and highest velocity magnitudes were observed at the realistic model with particle interaction case nearly the wall of the right lung side (larger than the left lung side) at 9.42 m/s to 10.47 m/s, while the velocity magnitudes at other areas are around 7.33 m/s to 8.38 m/s. In the real situation during inhalation, the inhaled particle can collide with each other. When having particle-particle interaction, the flow in that area will become more complex and turbulent. This can support the velocity pattern on the realistic

 doi:10.20944/preprints202211.0500.v1

model with particle interaction case that particle-particle interaction generates a high-velocity magnitude along the bifurcation. The details of particle-particle interaction are provided in the particle analysis section.

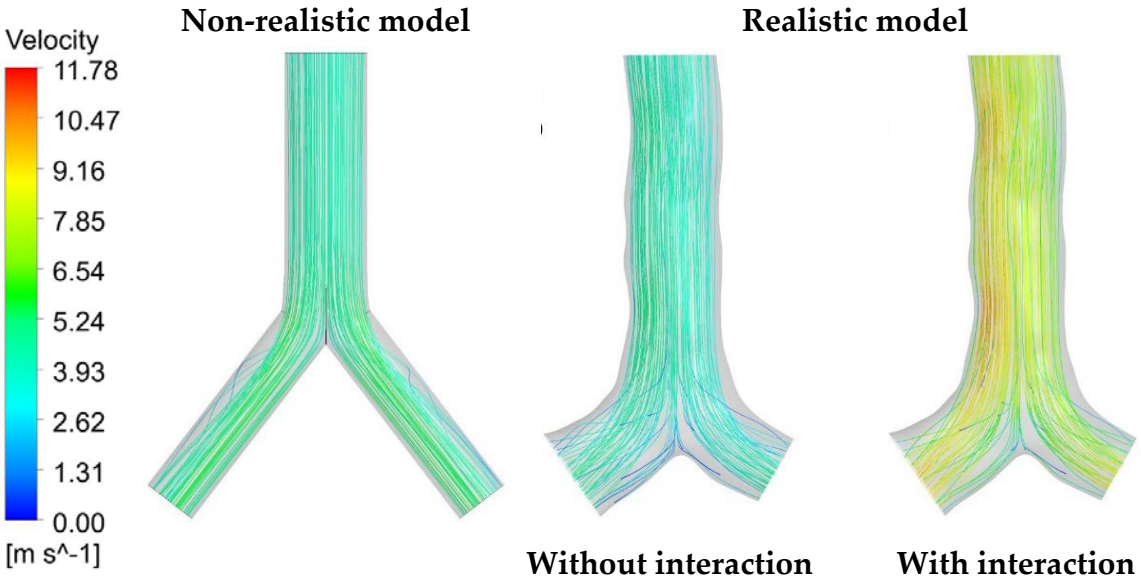

Figure 7. Velocity streamline for 60 lpm flow rate between non-realistic model and realistic model.

Velocity streamline for all three cases under the 60 lpm flow rate is presented in Figure 7 to provide a better understanding of the flow field dynamics inside the lung airway. From this figure, it is clear that particle-particle interaction significantly generates a higher flow velocity inside the domain compared to other cases. The highest velocity magnitude at 11.78 m/s was found in this case, while the highest velocity magnitude from other cases was observed to be lower than 7.85 m/s. From the non-realistic model, the highest flow was found at the central area of the left lung and right lung, while the lowest flow was found at nearly the wall of the airway. However, for the realistic model, the highest flow was observed on the right side instead. This can be because the complex structure of the realistic model affects the change in flow patterns during passing the airway.

1.1.2. Velocity Analysis for various selected parameters of the discrete element method (DEM)

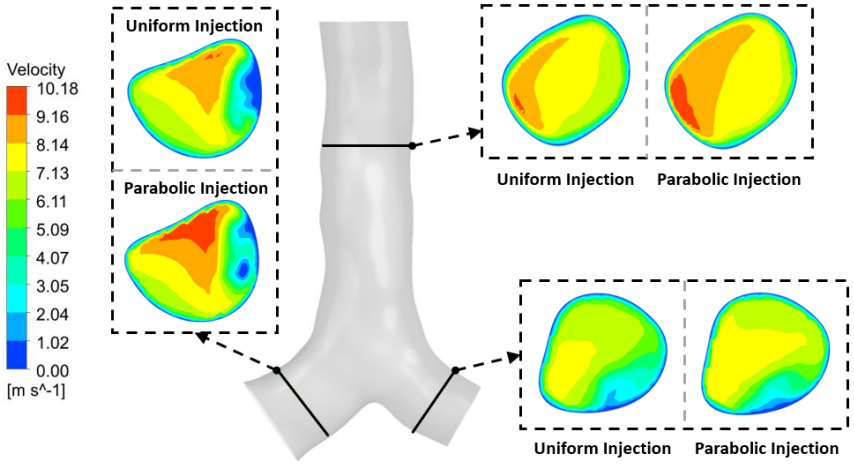

Figure 8. Velocity contour at three selected locations for different injection methods with 60 lpm flow rate.

Preprints (www.preprints.org) | NOT PEER-REVIEWED | Posted: 28 November 2022 doi:10.20944/preprints202211.0500.v1

In general, during inhalation, the flow field in the mouth-throat area is usually a uniform flow and becomes a parabolic flow at the trachea and upper airways (Gemci et al., 2008). In the CFD simulation, the airway walls were set as the no-slip boundary condition. This leads to having a parabolic flow in this field (Chen et al., 2021). To compare the flow characteristics between the uniform and parabolic velocity distribution, the velocity contours at three selected locations are created and provided in **Figure 8** under the DEM model with the flow rate at 60 lpm.

From this figure, it can be seen that a lower velocity magnitude usually locates at the wall of bifurcation for all selected locations. The higher velocity magnitude was found at the top plane and the left plane (represent the right lung due to having a larger size compared to another side). This can be because the airway characteristic is larger and more complex than the left lung. The maximum velocity magnitude from the left lung is lower than 8.14 m/s. However, the maximum velocity magnitude from another two locations is 10.18 m/s. Focusing on the flow patterns between these two methods, the parabolic injection method significantly generates a higher flow velocity for all selected locations, which results in the difference in flow patterns, especially at the right lung side.

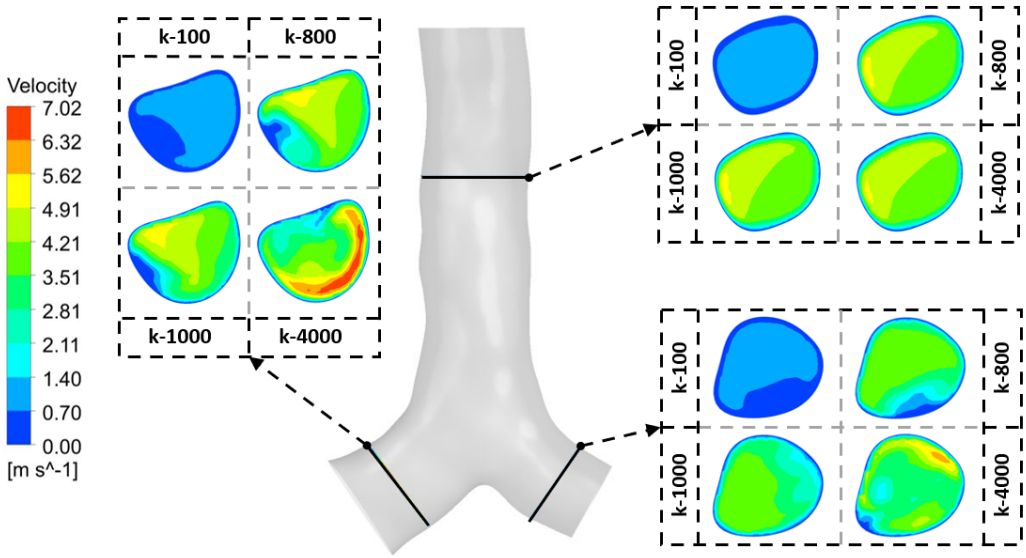

Figure 9. Velocity contour at three selected locations for different spring constants with 60 lpm flow rate.

In fact, the DEM is a numerical method that is used to model the interaction between individual particles and boundaries. When using DEM, the spring constant (k) in the contract force model of DEM is usually reduced for calculation time or calculation cost purposes. However, the reduction in spring constant significantly changes the agglomeration behaviour of cohesive particles (Toshitsugu & Kimiaki 2018).

To understand the effect of spring constant on the flow patterns of the human lung airway, the four selected spring constants are used as the input parameters under the flow rate at 60 lpm. **Figure 9** presents the velocity contours at three selected locations under different spring constants, including k-100, k-800, k-1000, and k-400. From this figure, it is clear that a higher spring constant significantly generates a higher flow velocity for all locations. From the spring constant at 100, the maximum velocity was found to be lower than 1.40 m/s for all locations. The velocity fields are similar for the spring constant at 800 and 1000 from the upper part (top plane) and right lung (left plane), while the velocity fields are different at the left lung (right plane). However, the maximum velocity magnitude from these two constants still does not exceed 5.62 m/s. The highest spring constant at 4000 significantly causes the difference in velocity patterns, especially at the right lung

Preprints (www.preprints.org) | NOT PEER-REVIEWED | Posted: 28 November 2022 doi:10.20944/preprints202211.0500.v1

(left plane). The maximum velocity at 7.02 m/s was found on this side near the right wall, while the second highest value at 6.32 m/s was found at the right wall of the left lung (right plane).

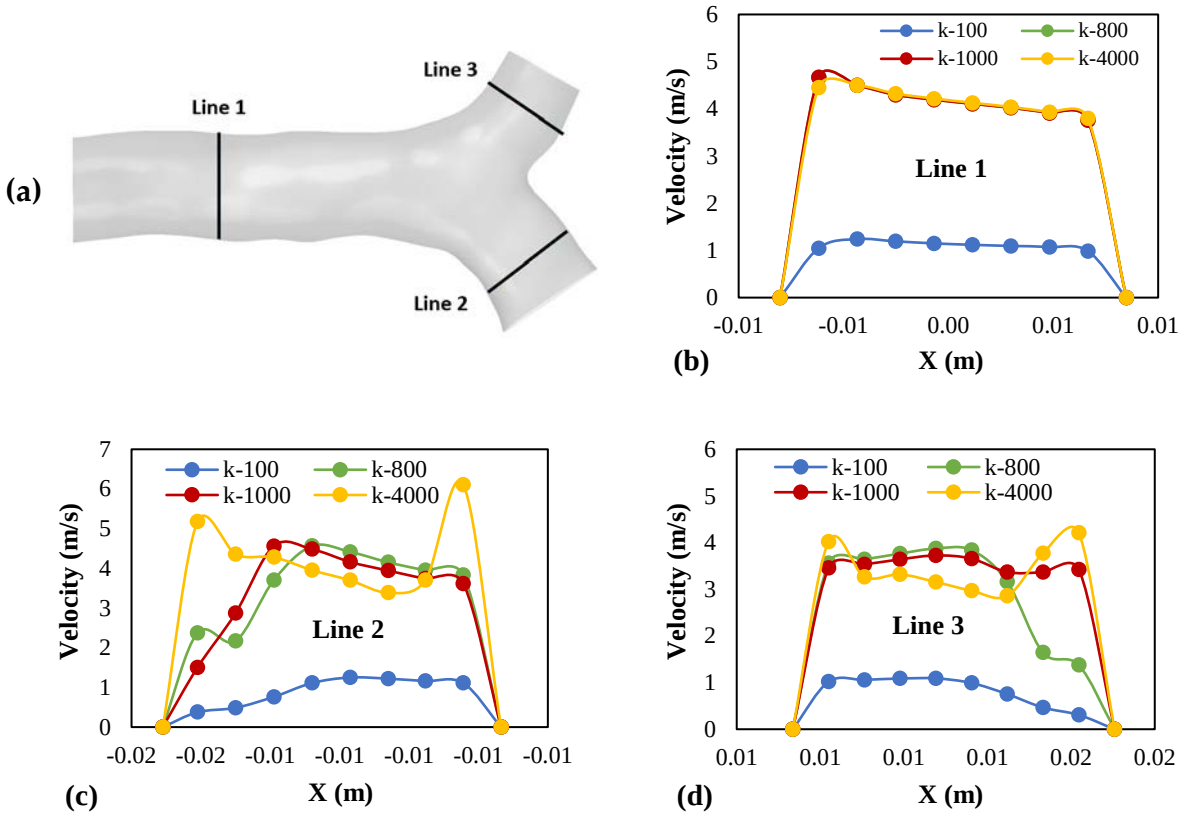

Figure 10. Velocity profile at three selected locations for different spring constants with 60 lpm flow rate. (a) selected locations of three lines, (b) velocity profile at line 1, (c) velocity profile at line 2, and (c) velocity profile at line 3.

To clarify the effect of spring constant on the flow pattern, the velocity profile is plotted at the same selected location from **Figure 9** and presented in **Figure 10** under the flow rate at 60 lpm. In general, the velocity profile represents the variation in velocity on a line at the right angles to the original flow's flow direction. This profile demonstrates the velocity magnitude and the change in the flow direction, which is caused by the different shapes within the domain (Larpruenrudee et al., 2021). With this technique, the flow's behaviour during transportation through the domain is easy to be evaluated. In this study, the velocity profile was plotted from the wall at the selected location to another side of the wall, as shown in **Figure 10a**. **Figure 10b-c** present the velocity profiles from Lines 1-3, respectively. From **Figure 10**, The flow pattern from Line 1 is a uniform flow for all spring constants, while Line 2 and Line 3 have a parabolic flow pattern. Furthermore, it is clearly seen that the velocity magnitude from the spring constant at 100 is significantly lower than other spring constants. From Line 1 (**Figure 10b**), the trend of the velocity profile is similar to the spring constant at 800 to 4000. However, at the right lung (Line 2) and left lung (Line 3), the trend of the velocity profile is totally different, especially at the 4000 of spring constant, which becomes more fluctuated near the wall. The discussion of the spring constants on particle deposition is provided in the particle analysis section.

1.2. Pressure Analysis

Non-realistic model **Realistic model**

 doi:10.20944/preprints202211.0500.v1

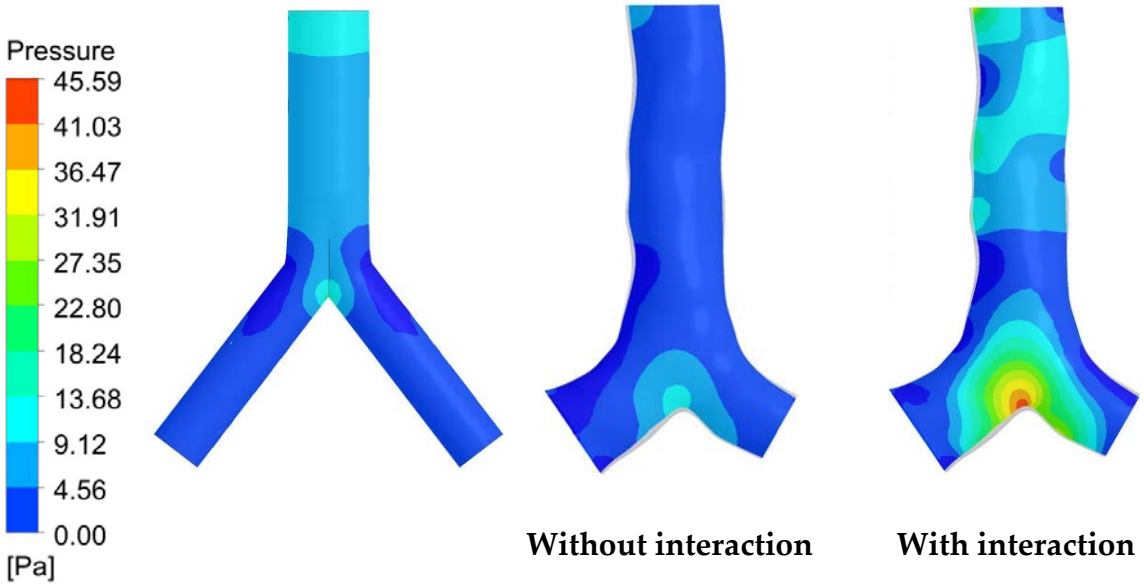

Figure 11. Pressure contour at X-Y Plane for 60 lpm flow rate between non-realistic model and realistic model.

The pressure variations inside the non-realistic and realistic lung airway are investigated and presented in **Figure 11** as the pressure contour under the flow rate at 60 lpm. In fact, pressure variation could be changed due to the effect of fluid flows during the domain. From this figure, it is clear that the pressure patterns between these three cases are different, especially in the non-realistic lung model. From the non-realistic model, the higher pressure was found at the inlet and the bifurcation area, while the left lung and right lung were found to have a lower pressure. From the realistic model without particle interaction, the higher pressure was observed at the left edge of the inlet and at the bifurcation area, while around nearly the right lung wall was found to have a lower pressure. However, the maximum pressure magnitude from these two cases is still lower than 13.68 Pa. When having particle interaction, a higher pressure was observed from several locations of the realistic model, especially at the left edge of the inlet and at the bifurcation area. The highest pressure at 45.59 Pa was noticed at the bifurcation area in this case. Referring to the velocity contour in **Figure 6**, the particle-particle interaction significantly affects the flow pattern inside the domain, which results in the change of pressure variation for this case compared to other cases without having particle interaction.

1.3. Wall Shear Analysis

Non-realistic model **Realistic model**

 doi:10.20944/preprints202211.0500.v1

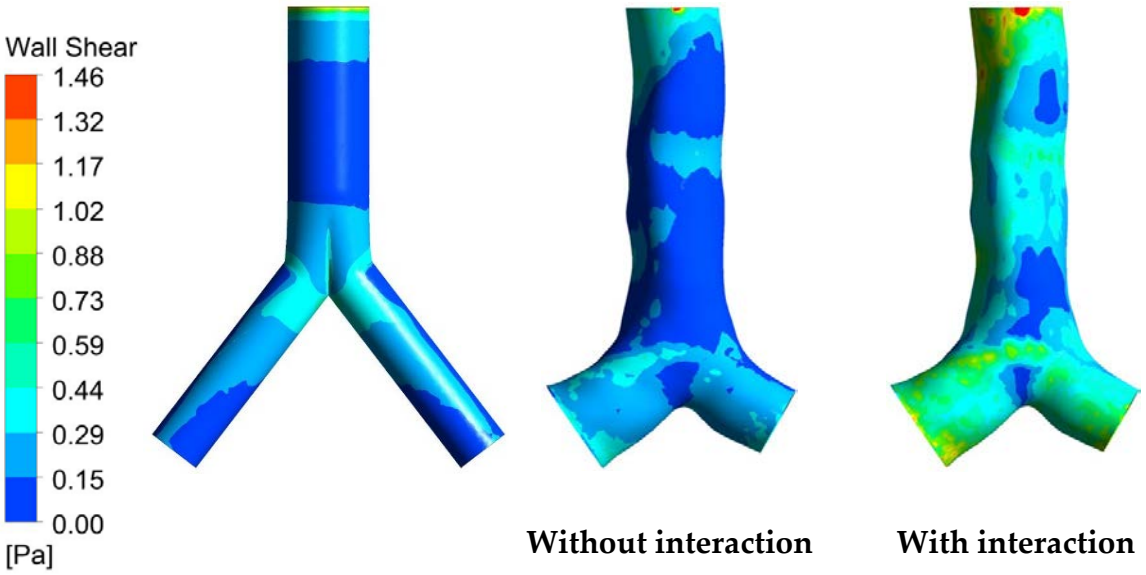

Figure 12. Wall shear stress contour at X-Y Plane for 60 lpm flow rate between non-realistic model and realistic model.

The shear stress on the wall of the lung airway is analyzed and presented in **Figure 12** under the comparison between non-realistic and realistic cases with 60 lpm flow rate. Wall shear stress refers to the shear stress of fluid which is usually occurring in the layer next to the wall of a domain (Larpruenrudee et al., 2021). Normally, the fluid flows fastest at the central area of the domain and flows slowest close to the wall of the domain. Due to the complicated structure of the realistic model, the variation of shear stress on the wall from this model is different from the non-realistic model. However, it can be seen the highest wall shear stress at 1.46 locates at the inlet area for all cases. The highest wall shear stress from other areas is still lower than 0.88 for the non-realistic model and realistic model without particle-particle interaction. At the right lung and left lung, the highest wall shear stress at 1.32 was found from the realistic model with particle-particle interaction.

2. Particle Analysis

Particle transport and deposition within the lung airways play an essential role in drug delivery. To obtain accurate results for particle transport and deposition, the comprehensive analysis of particle distribution and motion during transport within the human lung airways is significant. This can be done by numerical simulation based on the discrete element method (DEM). The numerical calculation from the DEM is generally based on Newton's second law, which will calculate the individual element's motion. The advantages of DEM are to consider friction, contact plasticity, gravity, cohesion and other interactions as well as record the information (position, velocity, forces exerted on) of each individual particle during the simulation (Chen et al., 2012). However, one of the main disadvantages of the DEM is a high computational demand as a high number of particles is usually involved for the real system, and each particle in the system must be tracked all the time (Branco Junior et al., 2015). Therefore, this section proposes a comprehensive analysis of particle transport and deposition under the DEM model for various initial

2.1. Particle with interaction and without interaction

Preprints (www.preprints.org) | NOT PEER-REVIEWED | Posted: 28 November 2022 doi:10.20944/preprints202211.0500.v1

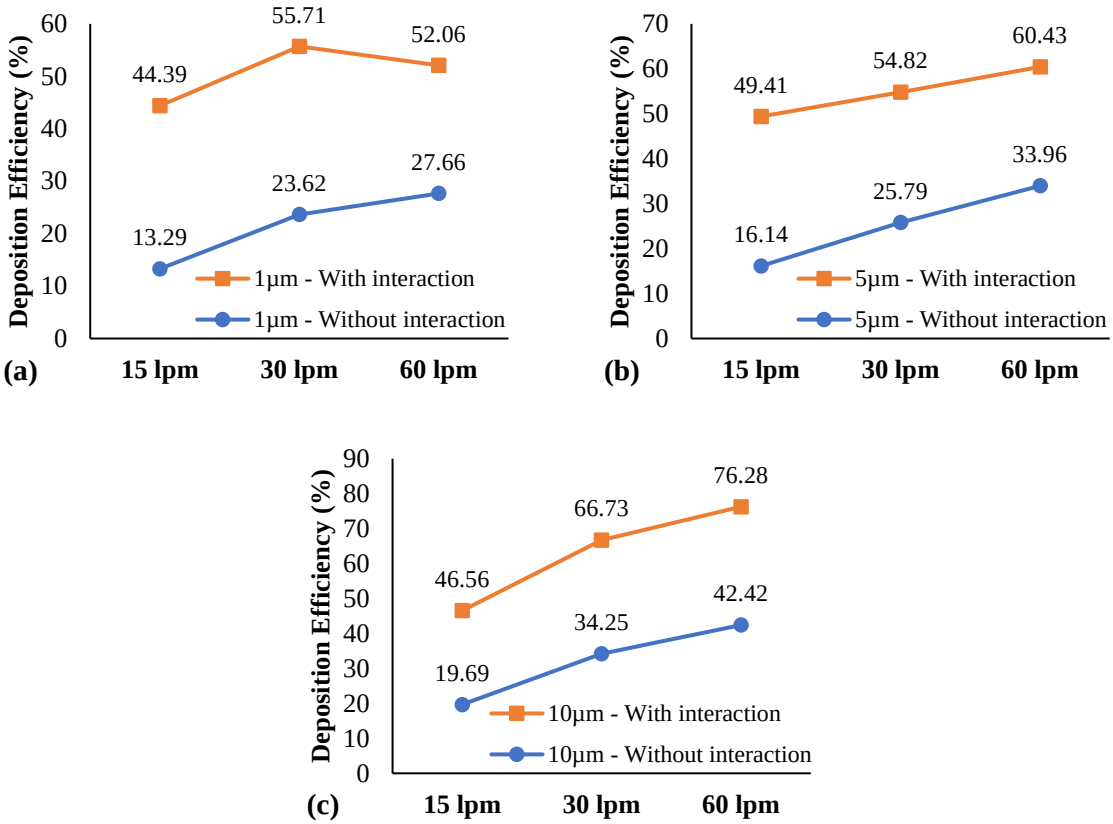

Figure 13. Particle DE between particle interaction and without interaction for various flow rates. (a) particle size at 1µm, (b) particle size at 5 µm, and (c) particle size at 10 µm.

The comparison of particle transport and deposition within the bifurcation for various flow rates and particle sizes is analyzed and presented as the particle DE (DE) in **Figure 13**. The numerical simulations were proposed based on the realistic lung model with and without particle-particle interaction. **Figure 13a-c** illustrate the DE from particle size as 1-10 µm, respectively. For the DE in this study, it refers to the percentage of total particles trapped during transportation through the domain which is divided by the total number of injected particles from the inlet of the domain. The remaining particles are classified as the escaped particles, which travel from the outlet of the right and left lungs. Basically, the DE is dependent on the particle diameter, flow rate, and density (Islam et al., 2021). For the microparticle, A greater particle diameter usually has a higher DE rate, while a higher flow rate generally results in a higher DE rate.

From the 15 lpm flow rate, the maximum DE was found to be lower than 20% and 50% for the case without particle interaction and with particle interaction, respectively. For the 30 lpm flow rate, the maximum DE was observed to be less than 35% and 67% from the case without particle interaction and with particle interaction, respectively. For the highest flow rate at 60 lpm, the maximum DE was noticed to be around 42% for the case without particle interaction and around 76% for the case with particle interaction. It can be seen that the results from the present study also support the above discussion that a higher flow rate results in a higher DE for both particle-particle with and without interaction and all particle sizes.

Focusing on the effect of particle size on the DE rate, it can be summarised based on the following discussions. For particle size at 1 µm (**Figure 13a**), the maximum DE from the case without particle interaction and with particle interaction was found to be less than 30% and 56%, respectively. From the particle size at 5 µm (**Figure 13b**) and 10 µm (**Figure 13c**), the maximum DE from the case without particle interaction was observed to

Preprints (www.preprints.org) | NOT PEER-REVIEWED | Posted: 28 November 2022 doi:10.20944/preprints202211.0500.v1

be less than 34% and 43%, respectively. However, for the particle size at 5 μm and 10 μm from the particle interaction cases, the maximum DE was found to be around 60% and 76%, respectively. It is obvious that a higher particle diameter results in a higher DE for all flow rates. This is because of the particle inertia which is higher from a larger particle size (van Ertbruggen et al., 2004; Ma & Lutchen 2009).

In addition, one of the most important things was observed that the DE from the case with particle interaction is significantly higher than the case without particle interaction, especially the case with 15 lpm flow rate and 1 μm particle diameter (around 1-time higher).

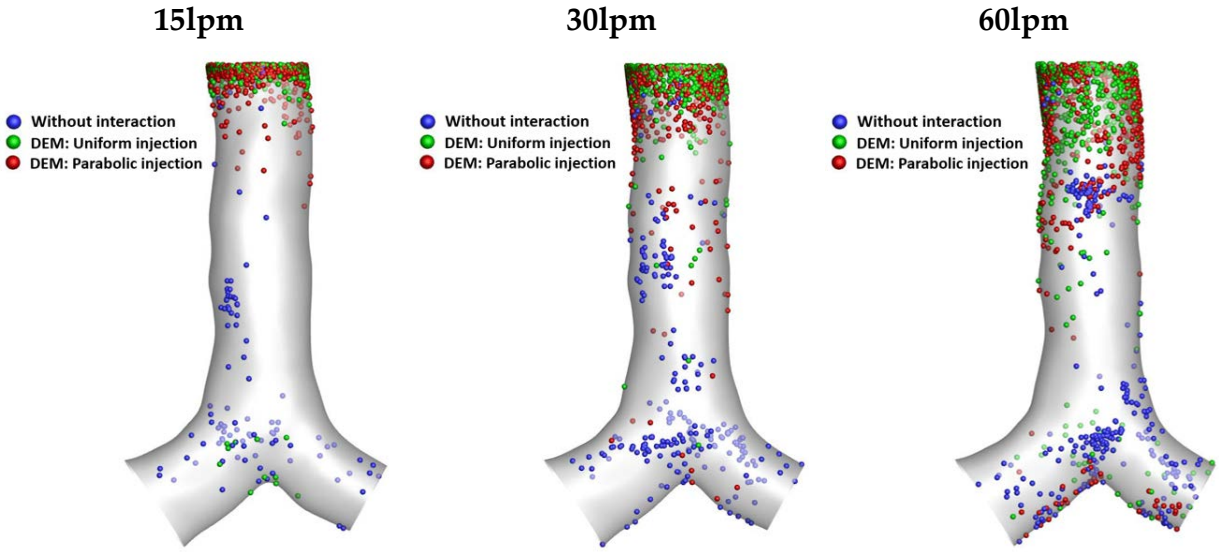

Figure 14. Particle deposition scenario for different injection methods for various flow rates with particle size at 10 μm.

To support the discussion of the DE from the case with and without particle interaction (refer to **Figure 13**), the particle deposition scenario was performed and presented in **Figure 14**. The blue particles refer to the case without particle interaction. The green particles and red particles refer to the case with particle interaction for uniform and parabolic injection of the fluid flow, respectively. It can be seen that a higher flow rate results in a higher particle deposition along the lung airway. Without particle interaction (blue particles), less particles are trapped at the inlet area, while most particles are trapped at the bifurcation. However, the cases with particle interaction have a higher particle deposition around the inlet area for both uniform injection (green particles) and parabolic injection (red particles).

2.2. Particle interaction for uniform injection and parabolic injection

15 lpm **30 lpm** **60 lpm**

Preprints (www.preprints.org) | NOT PEER-REVIEWED | Posted: 28 November 2022 doi:10.20944/preprints202211.0500.v1

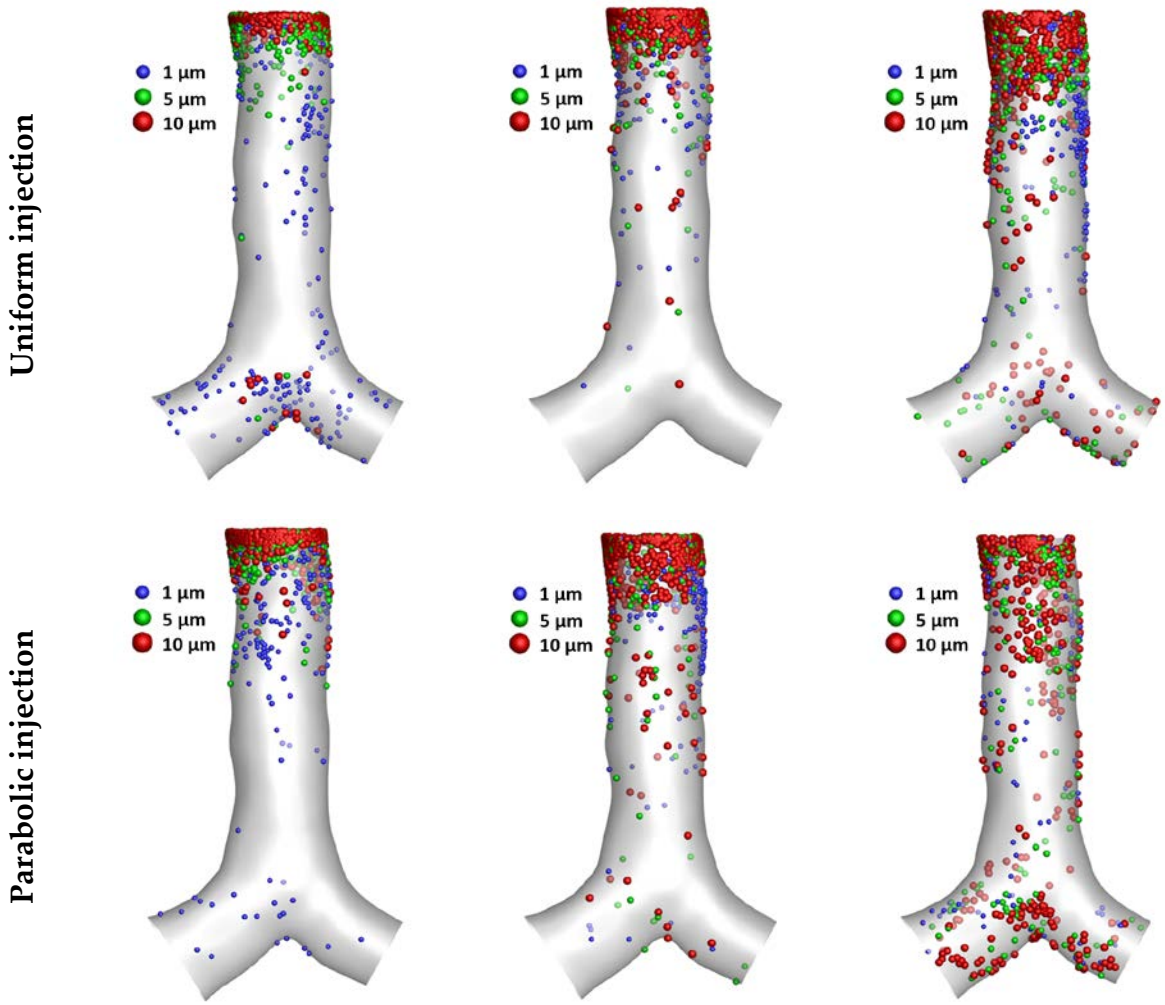

Figure 15. Particle deposition scenario between uniform injection and parabolic injection with spring constant at k-800.

The particle deposition scenarios from various flow rates and particle sizes were performed and presented (in **Figure 15**) under the uniform and parabolic injection of fluid flow. From **Figure 15**, it is clearly seen that most particles (all sizes) are usually trapped at the inlet area for all flow rates. Larger particle size is generally trapped at the inlet area, which results in a lower deposition at other areas, especially the particle size at 10 µm. However, a higher particle density concentration around the inlet area was found in the parabolic injection cases compared to uniform injection cases for all flow rates and particle sizes.

2.3. Particle interaction for different initial parameters

Table 2. Particle DE for various spring constants at 15 lpm flow rate and 10 µm.

Particle DE (%)							
k=50	**k=100**	**k=200**	**k=300**	**k=400**	**k=500**	**k=800**	**k=1000**
42.98	58.36	49.80	54.44	63.48	66.73	73.13	76.87

Table 2 shows the DE for different spring constants at 15 L/min flow rate. The overall DE shows an increasing trend with the spring constant. The numerical results report that the interaction between the particles is higher for the high spring constant values. When the interaction is higher, more particles deviate from the air streamline and increase the

Preprints (www.preprints.org) | NOT PEER-REVIEWED | Posted: 28 November 2022 doi:10.20944/preprints202211.0500.v1

overall DE. At k=50, the lowest DE is observed, while the highest DE is reported for k=1000.

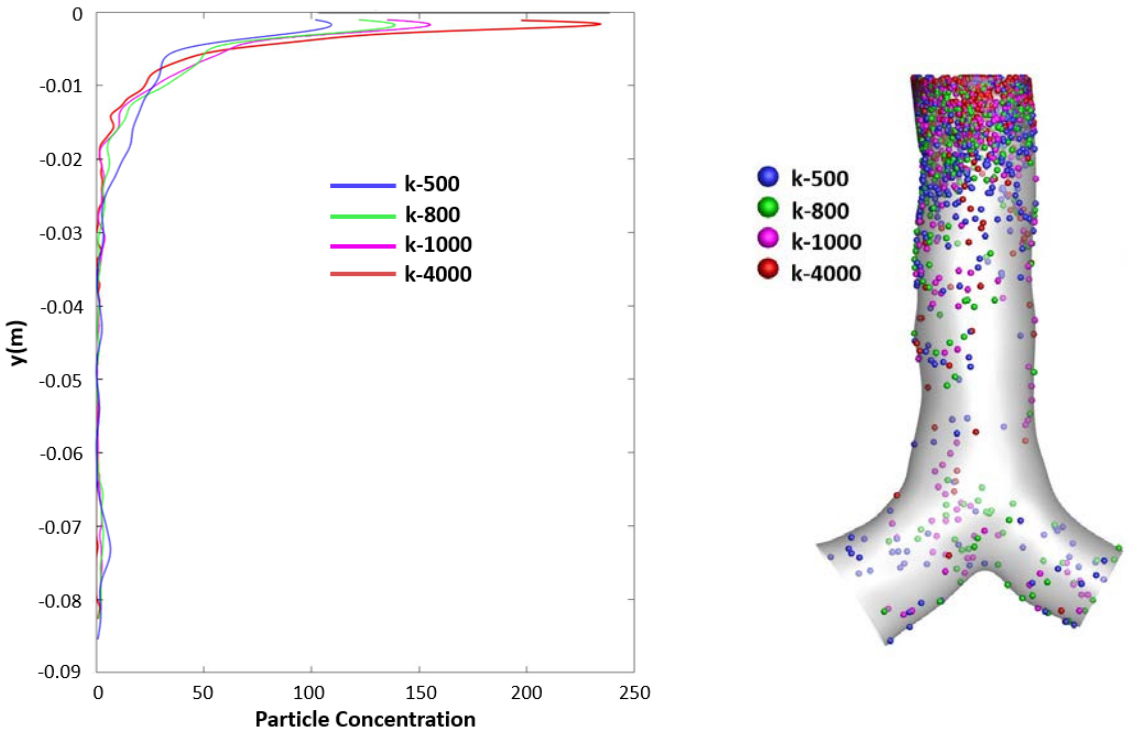

Figure 16. Particle deposition concentration and deposition scenario for different spring constants at 15 lpm flow rate. (a) particle deposition concentration and (b) particle deposition scenario.

As mentioned earlier regarding the effect of the spring constant on the velocity flow pattern, a higher spring constant will result in a higher velocity flow along the lung airway. **Figure 16** presents the particle deposition concentration (**Figure 16a**) and deposition scenario (**Figure 16b**) for various selected spring constants under the 15 lpm flow rate and 10 μm of particle size. The results from **Figure 16** could support the velocity flow pattern from **Figure 8** that the highest spring constant at 4000 has the highest particle density, while the lowest spring constant at 500 has the lowest particle deposition. From all cases, it can be seen that around the inlet area has a higher particle concentration.

Preprints (www.preprints.org) | NOT PEER-REVIEWED | Posted: 28 November 2022 doi:10.20944/preprints202211.0500.v1

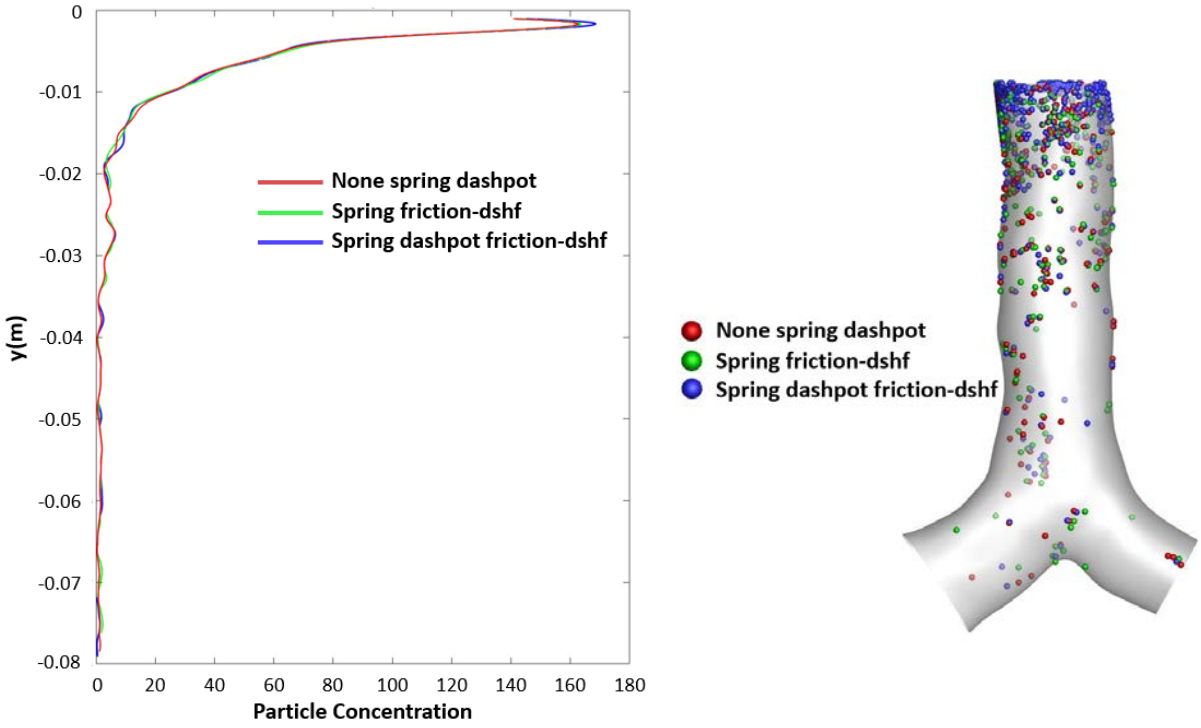

Figure 17. Particle deposition concentration and deposition scenario for different interaction methods at 15 lpm flow rate. (a) particle deposition concentration and (b) particle deposition scenario.

Figure 17 presents the particle deposition concentration (**Figure 17a**) and deposition scenario (**Figure 17b**) for different interaction methods at 15 lpm flow rate under the particle size at 10 μm. These methods include the none spring dashpot (red line and red particle), spring friction-dshf (green line and green particle), and spring dashpot friction-dshf (blue line and blue particle). From this figure, it can be seen that the trend of particle deposition concentration is similar for all cases that have a higher particle deposition at the inlet area. However, from the inlet area, the particle deposition concentration from the spring dashpot friction-dshf case (blue colour) was found to be slightly higher than another two cases, while other areas were found to be similar.

Conclusions:

The CFD-DEM model analyzed the flow and particle transport in the upper airway of an idealized and realistic airway model. Different inhalation methods and interaction methods are employed to analyze the particle transport behaviour. The key findings of the CFD-DEM model are listed below;

- The fluid flow field for the particle-particle interaction model is found significantly complex than the without-interaction model. The CFD model shows a uniform flow field in the upper part of the airways, while the CFD-DEM model shows the flow field is highly complex in the upper airways;
- The velocity profile for CFD-DEM model at various selected positions of the first bifurcation is highly complex than the CFD model. The uniform and parabolic inhalation method also shows the variation of the flow profiles;
- The higher value of the spring constant significantly influences the flow fields. With the high spring constant value, multiple vortices are generated at the upper airways;
- The overall DE for the particle-particle interaction model is higher than the without-interaction model. The DE also increases with the flow rate and particle diameter irrespective of the CFD and CFD-DEM models;

- Inhalation and injection method influences the DE in upper airways. For larger diameter aerosol and parabolic injection method, higher DE is observed at the upper part of the airways than uniform injection;
- For a high spring constant value, the particle-particle interaction is found significantly higher at the upper part of the first bifurcation. Higher deposition concentration is observed at the upper part of the airway, and the opposite scenario is observed for the lower spring constant value.
- The particle-particle interaction and DE at the upper part of the first bifurcation are found higher for the spring dashpot friction-dshf method than other interaction methods.

The study employed different interaction and injection methods and analyzed the flow fields and particle transport in upper airways. The findings of this study would improve the knowledge of particle interaction in airways. The present study and a more case-specific study would improve the knowledge of the CFD-DEM and particle transport behaviour in upper airways.

Acknowledgment: The authors acknowledge the iHPC support at UTS. The funding from the Australian Research Council (ARC DP210101353) is highly acknowledged.

Conflicts of Interest: No conflicts of interest associated with this study.

Data Statement Availability: Data will be available upon request.

Reference

1. Chen, W., Chang, C., Mutuku, J.K., Lam, S.S., Lee, W., 2021. Aerosol deposition and airflow dynamics in healthy and asthmatic human airways during inhalation, Journal of Hazardous Materials 416, 125856.
2. Chen, X., Zhong, W., Zhou, X., Jin, B., Sun, B., 2012. CFD-DEM simulation of particle transport and deposition in pulmonary airway. Powder Technology 228, 309-318.
3. Corda, J.V., Shenoy, B.S., Ahmad, K.A., Lewis, L., Prakashini, K., Khader, S.A., Zuber, M.J.C.M., 2022. Nasal airflow comparison in neonates, infant and adult nasal cavities using computational fluid dynamics. J Computer Methods Programs in Biomedicine 214, 106538.
4. Cundall, P.A., Strack, O.D.L., 1979. A discrete numerical model for granular assemblies. Geotechnique 29(1), 47–65
5. Feng, Y., Kleinstreuer, C., 2014. Micron-particle transport, interactions and deposition in triple lung-airway bifurcations using a novel modeling approach. Journal of Aerosol Science 71, 1-15.
6. Garcia, G.J., Bailie, N., Martins, D.A., Kimbell, J.S., 2007. Atrophic rhinitis: a CFD study of air conditioning in the nasal cavity. Journal of applied physiology 103, 1082-1092.
7. Ghahramani, E., Abouali, O., Emdad, H., Ahmadi, G., 2014. Numerical analysis of stochastic dispersion of micro-particles in turbulent flows in a realistic model of human nasal/upper airway. Journal of aerosol science 67, 188-206.
8. Gemci, T.; Ponyavin, V.; Chen, Y.; Chen, H.; Collins, R. Computational model of airflow in upper 17 generations of human respiratory tract. J. Biomech. 2008, 41, 2047–2054.
9. Heyder, J., Gebhart, J., Rudolf, G., Schiller, C.F., Stahlhofen, W., 1986. Deposition of particles in the human respiratory tract in the size range 0.005–15 μm. Journal of Aerosol Science 17, 811-825.
10. Inthavong, K., Zhang, K., Tu, J., 2011. Numerical modelling of nanoparticle deposition in the nasal cavity and the tracheobronchial airway. Computer Methods in Biomechanics and Biomedical Engineering 14, 633-643.
11. Islam, M.; Larpruenrudee, P.; Hossain, S.; Rahimi-Gorji, M.; Gu, Y.; Saha, S.; Paul, G. Polydisperse Aerosol Transport and Deposition in Upper Airways of Age-Specific Lung. Int. J. Environ. Res. Public Health 2021, 18, 6239.
12. Islam, M.S., Saha, S.C., Sauret, E., Ong, H., Young, P., Gu, Y., 2019. Euler–Lagrange approach to investigate respiratory anatomical shape effects on aerosol particle transport and deposition. Toxicol. Res. Appl. 3, 2397847319894675.
13. Islam, M.S., Paul, G., Ong, H.X., Young, P.M., Gu, Y.T., Saha, S.C., 2020. A review of respiratory anatomical development, air flow characterization and particle deposition, International Journal of Environmental Research and Public Health 17, 380.
14. Islam, M.S., Fang, T., Oldfield, C., Larpruenrudee, P., Beni, H.M., Rahman, M.M., Husain, S., Gu, Y., 2022. Heat wave and bushfire meteorology in New South Wales, Australia: air quality and health impacts. International journal of environmental research and public health 19, 10388.
15. Kleinstreuer, C., Zhang, Z., Li, Z., 2008. Modeling airflow and particle transport/deposition in pulmonary airways. Respiratory physiology & neurobiology 163, 128-138.

 doi:10.20944/preprints202211.0500.v1

16. Koullapis, P., Hofemeier, P., Sznitman, J., Kassinos, S.C., 2018. An efficient computational fluid-particle dynamics method to predict deposition in a simplified approximation of the deep lung. European Journal of Pharmaceutical Sciences 113, 132-144.
17. Larpruenrudee, P.; Islam, M.S.; Paul, G.; Paul, A.R.; Gu, Y.T.; Saha, S.C. Model for Pharmaceutical aerosol transport through stenosis airway. In Handbook of Lung Targeted Drug Delivery Systems: Recent Trends and Clinical Evidences; CRC Press: Boca Raton, FL, USA, 2021; pp. 91–128.
18. Ma, B., Lutchen, K.R., 2009. CFD simulation of aerosol deposition in an anatomically based human large-medium airway model. Annals of Biomedical Engineering 37, no. 271.
19. Murphy, K.R., Eivindson, A., Pauksens, K., Stein, W.J., Tellier, G., Watts, R., Léophonte, P., Sharp, S.J., Loeschel, E., 2000. Efficacy and safety of inhaled zanamivir for the treatment of influenza in patients with asthma or chronic obstructive pulmonary disease. Clinical Drug Investigation 20, 337-349.
20. Newman, S.P., 2005. Principles of metered-dose inhaler design. Respiratory care 50, 1177-1190.
21. Rahman, M.M., Zhao, M., Islam, M.S., Dong, K., Saha, S.C., 2022. Nanoparticle transport and deposition in a heterogeneous human lung airway tree: An efficient one path model for CFD simulations. European Journal of Pharmaceutical Sciences 177, 106279.
22. Sakagami, M., 2006. In vivo, in vitro and ex vivo models to assess pulmonary absorption and disposition of inhaled therapeutics for systemic delivery. Advanced drug delivery reviews 58, 1030-1060.
23. Sécher, T., Mayor, A., Heuzé-Vourc'h, N., 2019. Inhalation of immuno-therapeutics/-prophylactics to fight respiratory tract infections: an appropriate drug at the right place! Frontiers in Immunology 10, 2760.
24. Stahlhofen, W., Gebhart, J., Heyder, J., 1981. Biological variability of regional deposition of aerosol particles in the human respiratory tract. The American Industrial Hygiene Association Journal 42, 348-352.
25. Stahlhofen, W., Gebhart, J., Rudolf, G., Scheuch, G., 1986. Measurement of lung clearance with pulses of radioactively-labelled aerosols. Journal of Aerosol Science 17, 333-336.
26. Telko, M.J., Hickey, A.J., 2005. Dry powder inhaler formulation. Respiratory care 50, 1209-1227.
27. Toshitsugu, T., Kimiaki, W., 2018. DEM simulation of granular flow (reduction of calculation cost by reducing spring constant). Journal of the Society of Powder Technology 55(8), 455-460. 10.4164/sptj.55.455
28. Van Ertbruggen, C., Hirsch, C., Paiva, M., 2005. Anatomically based three-dimensional model of airways to simulate flow and particle transport using computational fluid dynamics. J Appl Physiol (1985) 98, no. 3, 970-980.
29. Vulović, A., Šušteršič, T., Cvijić, S., Ibrić, S., Filipović, N., 2018. Coupled in silico platform: Computational fluid dynamics (CFD) and physiologically-based pharmacokinetic (PBPK) modelling. European Journal of Pharmaceutical Sciences 113, 171-184.
30. Weibel, E.R., Morphometry of the human lung. New York: Springer Verlag and Academic Press, 1963.
31. Zhu, H.P., Zhou, Z.Y., Yang, R.Y., Yu, A.B., 2007. Discrete particle simulation of particulate systems: theoretical developments, Chem. Eng. Sci. 62, 3378–3396.